Ocean Engineering 339 (2025) 121655

Contents lists available at ScienceDirect

Ocean Engineering

journal homepage: www.elsevier.com/locate/oceaneng

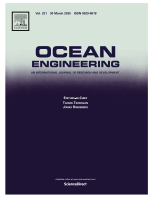

Research paper

Tuning body shape and stiffness to reduce water slamming forces

Bart Boom [a,1], Tadd Truscott [b], Frank E. Fish [c], Ed Habtour [a,*]

[a] The University of Washington, Seattle, 98105, Washington, USA
[b] King Abdullah University of Science and Technology, Thuwal, 23955, Saudi Arabia
[c] West Chester university, West Chester, 19383, Pennsylvania, USA

ARTICLE INFO

Keywords:
Fluid-structure interaction
Hydroelasticity
Water entry
Conical body
Energy flow
Nonlinear dynamics
Segmentation

ABSTRACT

This paper reveals how plunge-diving seabirds control impact energy during high-velocity water entry to hunt fish in deep waters without breaking their necks. Previous research has shown that the aerodynamic shape of the head or the structural compliance in the neck can reduce slamming forces. However, the physics governing their combined effects combined on the dive performance are is not well understood. The paper addresses this gap by demonstrating analytically and experimentally why the combined effect of shape and compliance is key for controlling the energy transmission during impact, passively. The impact forces at varying velocities are measured experimentally using a simple projectile design— to emulate seabirds' dives —with different head shapes (cone angles) and spring stiffnesses (compliance). The experiments are utilized to develop a semi-analytical model to estimate the amount and duration of the stored, released, and dissipated energy. Our findings show that the slamming forces can be passively reduced by tuning the compliance to increase the amount of impact energy stored in the system and delay its release and dissipation. While decreasing the cone angle reduces the slamming forces for a rigid system, the effect of compliance on reducing these forces is more pronounced in projectiles with half-cone angles larger than 30°. Modeling the interplay between cone angle and neck compliance offers physical insights into how diving seabirds mitigate mechanical stresses during impacts, thereby avoiding catastrophic damage. Conversely, these insights can be exploited to engineer mechanical systems with passive control of dynamic loads such as impact, shock, or vibrations with minimal energy losses.

1. Introduction

An object experiences large forces as it impacts the water at high velocity. Diving seabirds such as the Northern gannet (*Morus bassanus*) plunge through the surface at speeds around 70 mph, multiple times per day, to hunt. They have evolved to survive these impact forces by developing several features such as narrow beaks, compliant cervical (neck) anatomy and pressure-dissipative feathers (Weiss, 2014; Chang et al., 2016; Bhar et al., 2019; Sharker et al., 2019; Zimmerman et al., 2019; Zimmerman and Abdelkefi, 2020). Understanding the mechanics governing their remarkable impact mitigation can generate novel solutions for addressing important challenges in ocean engineering, such as improving the resilience of offshore wind turbines and oil rigs exposed to harsh ocean wave slamming (Paulsen et al., 2019), protecting boat hulls (Abrate, 2011), cushioning seaplane water-landing (von Karman, 1929), streamlining projectile water entry (Truscott et al., 2014), and enabling air-to-water transformer drones (Lu et al., 2024; Gan et al., 2024; Rockenbauer et al., 2021; Weisler et al., 2017).

Some of the first and most influential studies on measuring water impact forces include those by Thompson (1928), May (1970), Grady (1979). Researchers proposed a variety of approaches to reduce forces, such as the application of surface treatments (Aristoff and Bush, 2009; Truscott and Techet, 2009; Shokri and Akbarzadeh, 2022; Mehri and Akbarzadeh, 2021; Benschop and Breugem, 2017; Koeltzsch et al., 2002; Chen et al., 2014, 2013), air and water jets (Elhimer et al., 2017; Speirs et al., 2019) and creating cavities in front of the projectile (Guo et al., 2020; Lyu et al., 2021; Rabbi et al., 2021). Researchers have extensively studied various nose geometries, including hemispheres, ogives, cones, cusps, and cups to characterize the effect of geometry on water entry (Baldwin, 1971, 1975; Belden et al., 2023; McGehee et al., 1959; Thompson, 1965; Li and Sigimura, 1967; May, 1970; Qi et al., 2016; Sharker et al., 2019; Güzel and Korkmaz, 2020; Xu et al., 2011). All shapes were shown to exhibit a peak in the total drag coefficient due to slamming forces before settling into a steady state drag coefficient. The distinction lies in the nature of the transition: hemispheres and ogives display a rounded peak beginning at the moment of contact,

* Corresponding author.
E-mail addresses: bboom@uw.edu (B. Boom), habtour@uw.edu (E. Habtour).
URL: illimitedlab.com (E. Habtour)
[1] Lead author: Bart Boom.

https://doi.org/10.1016/j.oceaneng.2025.121655
Received 2 January 2025; Received in revised form 22 May 2025; Accepted 23 May 2025
Available online 4 July 2025

Symbol	Description
β	Half cone angle
C_d	Coefficient of drag
A_{max}	Maximal acceleration
t_{max}	Time at maximal acceleration
k	Spring stiffness
k_S	Spring stiffness soft spring 1.76 N/mm
k_F	Spring stiffness firm spring 8.16 N/mm
M	Mass rigid cone body
m_1	Mass body and spring
m_2	Mass of cone and bearing
m	Added mass
S	Depth below water surface
x	Displacement of body
c	Damping
d	Diameter cone
h	Height cone
F	Reaction force
g	Gravitational acceleration
H	Drop height
U_0	Impact velocity
ρ	Density
σ	Surface tension
ν	Kinematic viscosity
F_b	Buoyancy force
F_{C_d}	Drag force
F_g	Gravitational force
K	added mass coefficient
κ	Geometric mass coefficient
τ	Stabilization rate added mass
L_p	Depth at peak acceleration
E_0	Energy at impact
E_{rigid}	Total energy of rigid projectile
E_{sprung}	Total energy of sprung projectile
ΔE	Difference between rigid and sprung projectile
C	Force coefficient
I	Impulse

while cones and cusps exhibit a sharper peak during the transition from slamming to steady-state behavior (Baldwin, 1975). In previous studies, cone-shaped geometries have been examined to gain insight into the effect of the head shapes of diving birds on their ability to penetrate water surfaces at high velocities safely as studies show how the sharp angle of the beak has a lower peak load compared to non-diving birds (Chuang and Milne, 1971; Faltinsen and Zhao, 1998; Sharker et al., 2019; Weiss, 2014; Eliason et al., 2020). These results suggest that the morphology and structural anatomy of diving birds reduce impact forces and the risk of injury, as well as minimize drag to allow for deeper penetration and higher speed when capturing elusive prey (Sharker et al., 2019).

Research efforts also included experimental and analytical investigations of the effect of cone angle on impact forces (Baldwin, 1971; May, 1970; Shiffman and Spencer, 1951; Korobkin and Scolan, 2006; Scolan and Korobkin, 2001). May (1970) found that the drag coefficient, C_d, is an order of magnitude higher in a sharp cone projectile with half angle $\beta = 22.5^\circ$ ($C_d \sim 0.5$) than in a blunt shape with $\beta = 70^\circ$ ($C_d \sim 6$)— β is visually detailed in Fig. 1 and Fig. 2. Most analytical models available in the open literature focused only on blunt cones, i.e., cones with half angles between 70° and 84° (Malleron et al., 2007). These models do not hold for sharp cones that extend the period of impact. In fact, Sharker et al. (2019) found that the cone angle had a significant effect on the jerk, which is the time derivative of acceleration. They suggested that the diving birds' head shape evolved to reduce the potential damage from a high jerk. The jerk is an important metric in the transportation industry to assess the risk of passenger injury in crash

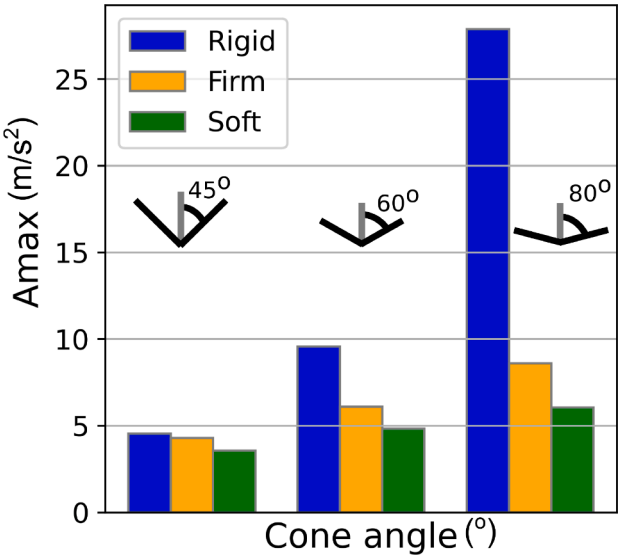

Fig. 1. Maximal accelerations (m/s^2) of rigid (no compliance) and firm, and soft sprung bodies at an impact velocity of 4.4 m/s.

testing; an in-depth description can be found in Hayati et al. (2020), Eager et al. (2016).

Limited studies have examined the water impact of a two-body system connected with a spring (Miller and Merten, 1952; Carcaterra and Ciappi, 2000; Wu et al., 2020; Antolik et al., 2023; Boom et al., 2023). Miller and Merten (1952) modeled hydrodynamic impact during seaplane water landings, where the aircraft structural stiffness was idealized as a linear spring. Carcaterra and Ciappi (2000) developed a nonlinear fluid-structure interaction model to predict peak forces for a two-mass wedge system that impacts water at hypersonic speed. Studies of the two-body sprung system with hemispherical shapes (Wu et al., 2020; Antolik et al., 2023; Boom et al., 2023). Wu et al. (2020) demonstrated experimentally that the impact force decreased with the introduction of a spring into a water entry system, but did not provide an analytical relationship between spring stiffness and impact forces. Antolik et al. (2023) showed that under certain conditions, adding a spring to the body could result in both force reductions and increases. Their experimental samples had different hemisphere radii and spring stiffnesses. Boom et al. (2023) experimentally compared the impact performance of a sprung system with hemisphere and 60°cone heads. They found that blunt shapes, in addition to hemispheres, greatly benefited from the addition of low spring stiffness by reducing maximal acceleration and jerk (Boom et al., 2023). The next step in understanding seabird diving was understanding the functional morphology of the neck. Computed tomography (CT) scans generated by Chang et al. (2016) suggested that the gannet neck S shape acts as a spring in compression along the midline. However, current research approximated the neck using continuous beam theory with uniform cross-sectional area (Chang et al., 2016; Zimmerman et al., 2019; Zimmerman and Abdelkefi, 2020). In this paper, we represent the neck as a sprung segmentation connecting the conical head to the body. This morphological analogy answers the following fundamental question: what is the influence of tuning both the stiffness of the neck, and the head geometry, on the energy distribution in the system? Our experimental results allowed us to develop a model to understand how to control the energy distribution and ultimately mitigate slamming forces.

We modeled the complex fluid-structure interaction by modifying the approaches of Carcaterra and Ciappi (2000), Aristoff and Bush (2009), Baldwin (1971). The model captures the unsteady effects of the hydraulic added mass and the varying water entry velocity. Additionally, we included contributions of steady-state drag, nose cone mass,

and body buoyancy. The steady-state drag due to viscous forces was experimentally estimated using least squares regression (Baldwin, 1971); details are provided in Appendix A. The peak force does not occur at full cone submergence for the cone-spring system, as suggested by most cone-only analytical models or wedge impact studies (Vincent et al., 2018). We extracted the energy flow between the projectile and the water, and the energy stored in the spring during impact. This revealed that the dissipation of impact energy can be manipulated to dissipate over a longer period, reducing peak loads. This model allows for the selection of spring compliance to best decrease body acceleration for a particular cone shape, and/or the selection of cone shape to best reduce head acceleration with a particular segmentation compliance Fig. 1.

The paper is structured as follows. Section 2 details the experimental setup and data acquisition. The modeling approach is provided in Section 3. Analyses and result discussions on the energy flow, water entry efficiency, and jerk are detailed in Section 4. In addition to the conclusion section, modeling details are included in Appendix A.

2. Methodology

2.1. Test cases

Each test projectile consisted of a head with a conical nose and a body which could be connected with either a spring or a rigid structure, as shown in Fig. 2b. The free body diagram of the system is detailed in Fig. 2b. Ten different cone angles between 10° and 80° are tested at five impact speeds between 2.2 and 5.4 m/s with rigid, firm, and soft connections. The range of cone angles was chosen to provide a broad representation from sharp to blunt shapes. A 12° angle was included based on the half-cone angle of the Northern gannet (Weiss, 2014). These experiments were designed to generate a comprehensive dataset to develop and validate the equation of motion for a system that encapsulates a wide range of cone angles and spring stiffnesses. Forces exerted on the body were calculated from the acceleration measurements obtained from an inertial measurement unit (IMU) mounted in the rear body; see Fig. 2a. The head and body were 3D printed using Polylactic acid (PLA), and Formlabs tough 2000 resin, respectively. The Formlabs resin was utilized to ensure waterproof internal housing. The dimensional tolerances of the FDM and SLA parts were −0.33 and −0.02 mm, respectively. The head geometry is depicted in Fig. 2c. The diameter, d, was kept constant at 52 mm. Cones with ten different half angles, β, between 10° and 80° were tested, as detailed in Table 1. The cone dimensions and masses for all samples are provided in Table 1. Each rear body was connected rigidly or with either a firm or a soft spring, where the stiffness constants for the firm and soft springs were $k_S = 1.74$ N/mm and $k_F = 8.16$ N/mm, respectively. The vendor stiffness values for each spring were confirmed by calculating the slopes of the force response plots obtained from compression loading tests using an Instron material testing system.

To ensure that the cone moved only along the body vertical axis, the nose motion was constrained with a linear bearing, which had minimal stiction but exhibited a small amount of viscous damping. The bearing housing was connected to the cone; as such, the nose and body masses can be computed as $m_2 = m_{cone} + m_{\text{linear bearing}}$, and $m_1 = m_{body} + m_{spring}$, respectively. The mass of each component in the projectile is provided in Table 2 and Table 1, which are used to normalize all the results. Releasing the sample into the water was achieved using an electromagnetic controller, where a steel plate mounted on the rear body tail could be attached to it.

All cone angles were tested for the rigid case, but only a selection of cone angles of 25, 45, 60, and 80° were tested with springs. Angles lower than 25° were not tested since the contribution of the spring to the entry dynamics became negligible at the tested speeds. Data are available on Github (Boom et al., 2025).

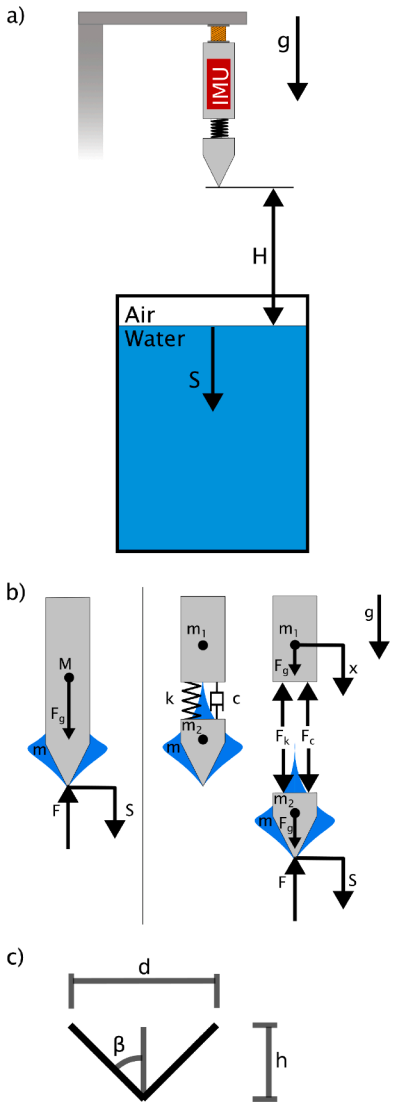

Fig. 2. a) Schematic of the experimental setup, where H and S are the drop height and depth traveled by the projectile, respectively. The drop release is controlled using an electromagnetic device shown in orange. The projectile is accelerated by gravity. The untethered inertial measurement unit (IMU) housed in the rear body is utilized to collect and store acceleration measurements. b) Free body diagram of rigid and sprung projectiles, where M, m, m_1, m_2, S, F_g, F, k, c, g are the mass of the rigid projectile, added mass, mass of body 1, mass of body 2, depth, gravitational force, water reaction force, spring stiffness, damping coefficient, and gravitational acceleration, respectively. c) cone diameter, half-angle, and height are d, β, and h, respectively. The range of β is 10° to 80°.

Table 1
Cone dimensions and masses.

Half angle (deg)	h_{cone} (mm)	Mass (g)
10	147.4	45.8
12	122.3	43.6
25	55.8	31.2
30	45.0	28.3
40	31.0	32.1
45	26.0	30.1
50	21.8	30.7
60	15.0	30.0
70	9.5	28.0
80	4.6	25.7

2.2. Experimental procedure

Each sample was dropped at different heights, H, using an electromagnet. The dropped samples were accelerated by gravity, as shown in Fig. 2a. The height was varied between 0.25 and 1.5 m to achieve impact velocity $U_0 \approx \sqrt{2gH} \approx 2.2$ to 5.4 m/s, respectively. The bodies were dropped into a round tank with internal dimensions of 895 × 514 mm ($H_{\text{tank}} \times D_{\text{tank}}$). The wall effects were neglected since the ratio of the dropped body diameter, d, and the tank diameter, D_{tank}, was $d/D_{\text{tank}} \approx 1/10$ (Guo et al., 2020). Acceleration measurements were collected using enDAQ IMU, Model: S2000D40, which had triaxial accelerometer with a sampling frequency of 4000 Hz, 8×10^{-5}g resolution, and less than 0.01gRMS noise level. The IMU sampling rate is comparable to studies reported in the literature (Sharker et al., 2019; Wu et al., 2020).

It was necessary to estimate four non-dimensional numbers: the Weber number (We), Froude number (Fr), Reynolds number (Re), and Bond number (Bo) to understand the dominant hydro effects included in the analysis. They are defined as $We = \rho d U_0^2/\sigma$, $Fr = U_0/\sqrt{gd}$, $Re = U_0 d/\nu$, and, $Bo = We/Fr^2 = \rho g d^2/\sigma$, where the water density is $\rho = 1000$ kg m^{-3}, surface tension of the air-water interface is $\sigma = 70\times10^{-3}$ Nm^{-1}, gravitational constant is $g = 9.81$ ms^{-2}, kinematic viscosity is $\nu = 10^{-6}$ m^2 s^{-1} and characteristic diameter is d. The resulting ranges were $We = 3.6\times10^3$ to 22×10^3, $Fr = 3.08$ to 7.56, $Re = 1.1\times10^5$ to 2.8×10^5, and $Bo = 378.9$. The high Weber number meant that the inertia of the displaced water was much more significant than the surface tension forces, which could be neglected. The hydrostatic and viscous forces could not be neglected due to low Fr and transition Re, respectively. The Bond number, which compares the strength of the surface tension to the gravitational forces, confirmed that the system was unaffected by surface tension.

3. Model development

This section details the unsteady-state semi-analytical model for estimating the water impact forces for ten different half cone angles ranging from 10° to 80°, see Table 1. The objective of the model is to describe the effect of the cone angle on the spatial and temporal evolution of the hydrodynamic forces starting from the initiation of water impact to the air cavity collapse. The model was experimentally validated, where each experiment was repeated six times.

3.1. Estimating impact forces

The model in this study includes the added mass effect, total drag, gravitational acceleration, and buoyancy but neglects surface tension effects due to a high Bond number; details are given in Section 2. The force balance thus becomes

$$(M + m(S))\ddot{S} + F_b + F_{Cd} = -F_g \tag{1}$$

where M, m, S, F_b, F_{Cd}, and F_g represent the mass of the object, the added mass, the depth of the cone, buoyancy force, drag force, and gravitational force, respectively. The gravitational and buoyancy forces are defined as;

$$F_g = Mg \tag{2}$$

Table 2
Component masses.

Part	Mass (g)
Body	522.8
Linear bearing	34.3
Rigid piece	2.5
Firm spring	4.0
Soft spring	1.5

$$F_b = \rho g V_s(S) \tag{3}$$

where g and ρ are the gravitational acceleration and density of the fluid, respectively. The submerged volume $V_s(S)$ is a function of the depth;

$$V_s(S) = \pi \tan\beta^2 \times \begin{cases} \frac{1}{3}S^3 & 0 \le S < h_{cone} \\ Sh_{cone}^2 - \frac{2}{3}h_{cone}^3 & h_{cone} \le S < h_{cone} + h_{body} \\ h_{body}h_{cone}^2 - \frac{2}{3}h_{cone}^3 & S \ge h_{cone} + h_{body} \end{cases} \tag{4}$$

where β, h_{cone}, and h_{body} are the half cone angle and the height of the cone and the body, respectively. The drag coefficient estimation incorporates both steady-state and unsteady-state components. The unsteady-state drag coefficient is based on the change in added mass;

$$F_{Cd} = \frac{\rho}{2} C_d(S) A_b(S) \dot{S}^2 \tag{5}$$

where,

$$C_d(S) = C_{ds} + C_{du} = C_{ds} + \frac{2}{\rho A_b(S)} \frac{dm}{dS} \tag{6}$$

where C_{ds} and $A_b(S)$ are steady state drag coefficient and the cone projected surface as a function of the depth S. The first term in Eq. (1) represents the inertia term, which depends on the acceleration of the mass and the projectile's added mass. Baldwin (1971) and Vincent et al. (2018) found the largest change in the added mass peaks before the full cone submersion. Therefore, the parameter L_p, is defined as the depth at peak acceleration. The added mass before L_p was classically defined by Shiffman and Spencer (1951), while the mass evolution beyond L_p is based on the work of Baldwin (1971). The evolution of the added mass is therefore defined as;

$$m(S) = \begin{cases} \rho K\left(\frac{d}{2}\right)^3 = \rho K(S\tan(\beta))^3 = \rho\kappa S^3, & S < L_p \\ \frac{6}{\tau^2}\rho\kappa L_p^3\left(1 - e^{-\tau\sqrt{\frac{S}{L_p}-1}}\left(\tau\sqrt{\frac{S}{L_p}-1}+1\right)\right), & S > L_p \end{cases} \tag{7}$$

where K is the added mass coefficient. We also introduce $\kappa = K\tan\beta^3$ as geometric mass coefficient, which combines the geometric and added mass coefficients to express the equation in terms of S. The parameter τ defines the added mass stabilization rate to its steady-state value. For completeness, the change in added mass can be obtained by taking the mass derivative with respect to S:

$$\frac{dm}{dS} = \begin{cases} 3\rho\kappa S^2 & S < L_p \\ 3\rho\kappa L_p^3 e^{-\tau\sqrt{\frac{S}{L_p}-1}} & S > L_p \end{cases} \tag{8}$$

To calibrate the model, a regression procedure is performed for variables κ, L_p, and τ to achieve the best curve fit for the experimental data. See Appendix A for more details.

3.2. Dynamics model

The water impact forces of segmented bodies connected by springs can be estimated using nonlinear ordinary differential equations. The model can be applied to a multi degree-of-freedom system because all external force parameters are functions of the position and velocity of the cone. We assume that the water can only exert forces on the cone since this is the only part that touches the water due to the air cavity around the body, as shown in Fig. 7a. Therefore, the equation of motion of the two bodies can be written as:

$$\begin{aligned} m_1\ddot{x} + c(\dot{x} - \dot{S}) + k(x - S) &= F_{g1} \\ M_2\ddot{S} + c(\dot{S} - \dot{x}) + k(S - x) + F_{cd} + F_b &= F_{g2} \end{aligned} \tag{9}$$

where x is the positions of the body and cone, see Fig. 2. Furthermore, c and k are the damping coefficient and spring stiffness. This formulation

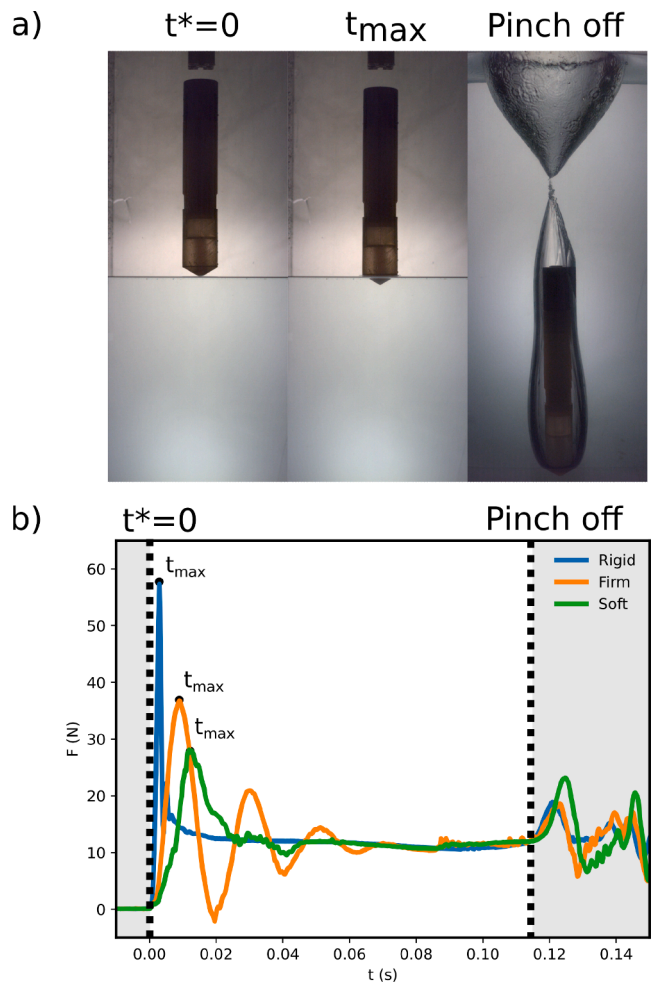

Fig. 3. a) Highlights three important events during impact: i) $t = 0$ initial impact; ii) t_{max} time of maximal force; and iii) t_p Pinch-off, the point where the cavity collapses. b) Shows the evolution of the forces acting on the rear body. Test cases are for rigid and firm, and soft sprung bodies with spring constants = 7.8 and 1.7 N/mm, respectively. The time stamps of the three impact events are divided by the dotted lines. The highlighted test corresponds to a half-cone angle of 60°at an impact speed of 4.4 m/s. The maximum force measurements for the rigid, firm, and soft configurations were 55.3 ± 1.5 N at 3.1 ± 0.1 ms, 35.6 ± 0.6 N at 9.0 ± 0.1 ms, and 28.2 ± 2.9 N at 8.1 ± 1.6 ms, respectively.

maintains the same functions for F_{Cd} and F_b as Eqs. (5) and (3), respectively. F_{g1} and F_{g2} are the gravitational forces of the body and head masses m_1 and m_2, respectively.

The importance of the formulation Eq. (9) is that it accurately estimates the projectile dynamics, since it captures the temporal evolution of the hydrodynamic mass, damping, and stiffness, starting from the initiation of impact. Therefore, the hydrodynamic coefficients must be updated for every time step. This is because during an unsteady condition, the projectile velocity changes, and subsequently, the impact forces change. The hydrodynamic damping and stiffness forces ramp up while oscillating over time, followed by fluctuating decay. For example, the buoyancy force oscillates due to compression and stretching of the projectile volume in response to spring oscillations. Similarly, the drag force experiences periodic decay due to the harmonic velocity response as a consequence of the compression and extension of the spring. The added mass experiences similar fluctuating dynamics. From an energy perspective, a detailed discussion of oscillatory behaviors is provided in Section 4.2.

4. Results and discussion

4.1. Impact characteristics and limitations

The impact of the conical body has three points of interest during water entry: i) initial impact at $t = 0^+$; ii) followed by maximum deceleration of the body at t_{max}; and iii) pinch-off at t_p, the point where the cavity collapses, as shown in Fig. 3. At initial impact, the projectile reaches the maximum kinetic energy, which is consequently reduced by the drag forces during water entry. The maximal force to the body is highest before full cone submersion for rigid projectiles and changes with cone angle. The body peak forces in the sprung projectiles can be delayed by reducing the spring stiffness, see Fig. 3. The forces after the peak decay to a steady state until pinch-off.

Fig. 4 The slamming forces are presented for blunt cones with half-angles 25, 45, and 80° during impacts for rigid samples. Sharper cones with half-angles less than 25° do not experience such large initial slamming forces; instead, they exhibit a gradual increase in force upon entering the water until reaching a steady state at the water entry speeds tested. Additionally, it can be seen that increasing velocity amplifies the impact force and shortens the time to peak force. When comparing rigid and sprung impacts, the impact force on the body is drastically reduced in most cases and stretched over time. It can be seen that the impact of the 25° increase in peak force.

4.2. Energy flow in the system

The model developed in Section 3.1 was utilized to calculate the energy flow and distribution in solid bodies. The energy flow is defined as the change in the energy over the water penetration depth. The energy experienced by the system consists of:

$$E_0 = \frac{1}{2} m U_0^2, \quad \text{where} \quad m = m_1 + m_2 \tag{10}$$

$$E_{rigid} = \frac{1}{2} m \dot{S}^2 \tag{11}$$

$$\begin{aligned} E_{sprung} &= E_k + E_p \\ &= \frac{1}{2}(m_1 \dot{x}_1^2 + m_2 \dot{S}^2 + k(x_1 - S)^2) \end{aligned} \tag{12}$$

$$\Delta E = E_{sprung} - E_{rigid} \tag{13}$$

where, E_0, E_{rigid}, and E_{sprung} are the initial energy at impact, $t = 0^+$, and total energy for the rigid and sprung systems, respectively. To compare the energy of the rigid and segmented projectiles, ΔE is calculated as the difference between E_{rigid}, and E_{sprung}. E_{sprung} is the sum of the kinetic energy due to the projectile inertia and the potential energy of the spring required to restore the system back to equilibrium. It was assumed that the potential energy due to buoyancy for the rigid and the sprung cases were equal, due to having the same volume. Therefore, the buoyancy effects were omitted from Eq. (12). Fig. 5 illustrates the energy flow in the system, normalized by E_0, as a function of depth for 25°, and 80° cases with and without springs. These two extreme cone angles were chosen to provide a succinct discussion of the most efficient and least efficient angles for water entry, which were 25°, and 80°, respectively.

The energy shown in Fig. 5a is calculated from depth starting at impact $S = 0.0$ to $S = 0.3$ until the whole body is submerged. From depth $S = 0.0$ to $S = L_p$, at peak acceleration, it can be observed that the energy dissipates significantly faster for a projectile with blunt angles than sharp ones, see $\beta = 80°$, and 25°. The drop in the total energy for the rigid and sprung projectiles at peak force are 15% and 7 %, respectively. Hence, projectiles with the 25° head continue accelerating for the rigid and sprung systems at initial impact. This is because the gravitational force is higher than the drag.

After $S = L_p$ is reached, the total energy decreases linearly for the rigid projectiles regardless of head angle size, see Fig. 5a. However, the

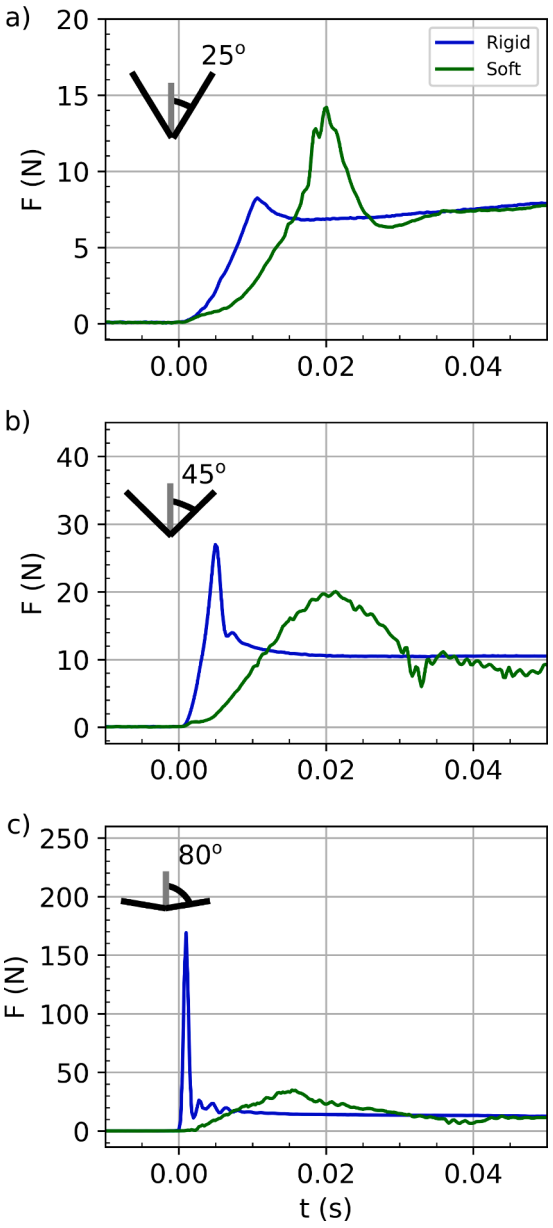

Fig. 4. Impact forces of half cone angles 25°, 45°, and 80° at impact velocities 4.4 m/s for rigid and soft spring.

total energy drops fluctuate harmonically for sprung systems with large β when they exceed the peak acceleration depth, $S > L_p$. These fluctuations are compared with the rigid cases in Fig. 5b by showing $\Delta E/E_0$ as a function of the depth, S. A positive $\Delta E/E_0$ means that a sprung system has retained more energy than the rigid one at the same depth. The energy fluctuation amplitudes for the sprung projectile with 80° cone are significantly higher than those with 25° cone regardless of the spring stiffness. Thus, introducing springs into a sharp cone projectile does not appear to have a significant effect on the energy flow. The maximum ΔE for 80° with firm and soft springs are 15 % and 13 % higher than those for 25°, respectively (Fig. 5b). The energy fluctuations in the system are higher for the $\beta = 80°$ than the cone angles of 25° due to the higher impulse force, see Fig. 6; therefore, the spring can absorb more energy and reduce the peak force more effectively.

Fig. 5c and d show the evolution of the kinetic and potential energy, respectively, as a function of depth for rigid and sprung projectiles with 25°, and 80° nose angles. The potential energy could be thought of as the kinetic energy that can be stored in the spring as a function of its compressive stiffness. One of the most important observations in the energy analysis is the asymmetric fluctuations in both the kinetic and potential energy of all sprung systems. The asymmetric decay is attributed to the simultaneous energy transfer between kinetic and potential, while energy losses are experienced as a result of drag. When the spring is compressed, the body length shortens, and its absolute velocity becomes lower than that of the rigid case, reducing drag forces.

In contrast, the spring extension stretches the body length, causing an increase in the drag forces. This explains the time lag in energy losses, which would not have been possible if we assumed constant velocity during water entry for segmented bodies, as suggested by recent studies. Therefore, the change in velocity, even for a short period, cannot be

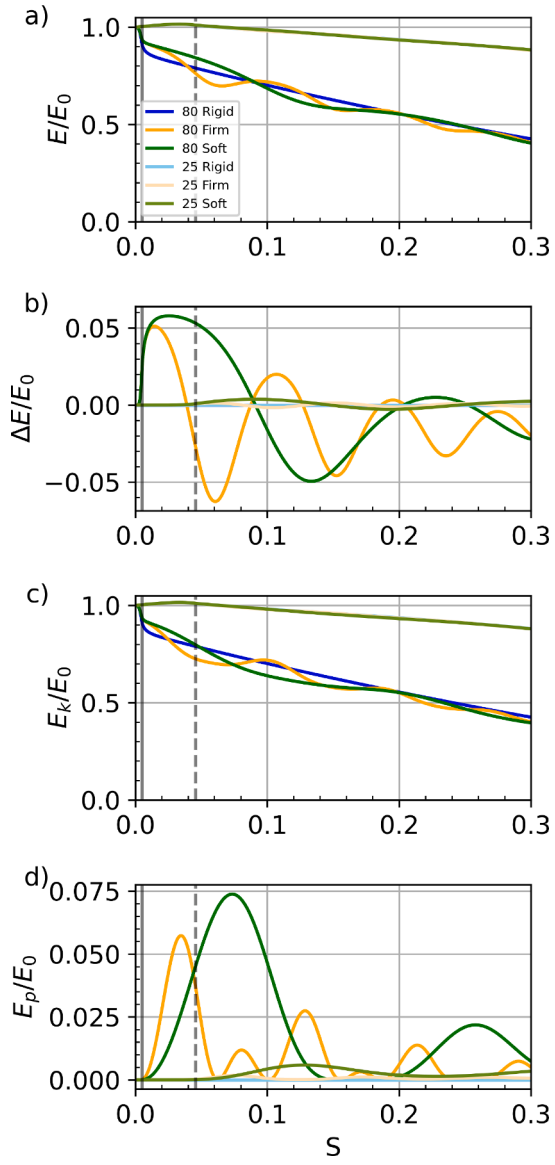

Fig. 5. The energy flow of two cone angles and the three stiffnesses are shown. a) shows the total energy in the system from the initiation of water impact until full submerging. b) is the energy difference between the rigid and the sprung cases; here, a positive value means that less energy is dissipated in the sprung system compared to its rigid counterpart and vice versa. c) and d) are the kinetic and potential energy, respectively. The energy in all plots is normalized by the initial energy E_0, i.e. at depth $S = 0.0$. The solid and dashed gray vertical lines are the L_p of 80°, and 25°, respectively. Note that the three lines corresponding to a half cone angle of 25° are very similar and overlap in subfigures a and c, but exhibit more noticeable differences in subfigures b and d.

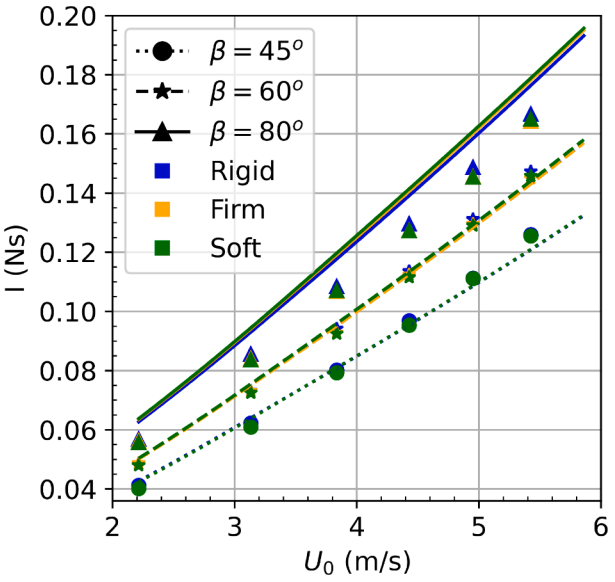

Fig. 6. Impulse of water entry as a function of the initial velocity for different cone angles and spring stiffnesses. The blue, orange, and green colors represent the rigid, firm, and soft springs, respectively. The solid, dashed, and dotted lines are the model results for $\beta =$ 80°, 60°, and 45°, respectively. The triangle, star, and circle markers are calculated from the experiments for $\beta =$ 80°, 60°, and 45°, respectively.

ignored for a high acceleration event since the drag force is constant. For completeness, it is worth mentioning that internal mechanical friction forces between the head and the body existed and contributed to energy losses. To this end, it was necessary to estimate the efficiency of an impulse to approximate the energy losses in the system, which is discussed in Section 4.4.

These findings are characteristic of the entire cone angle range. Cones with half-angles of 25° and below do not exhibit large changes in energy fluctuation compared to their rigid counterparts. The effect of the spring becomes more pronounced as the cone angle becomes blunter, as shown in Section 4.3.

4.3. Head shape and body stiffness influence on impact forces

The force coefficient of the body is calculated as the maximal acceleration times the mass of the body, expressed as $C = m_1\ddot{x}_1/((\rho A_{max}U_0^2)/2)$, which is a simplified measure of the drag coefficient over time during impact normalized by the projected area (A), weight and velocity of the projectile. Furthermore, the force coefficient of the head is defined differently, since the forces act on it in two directions. The impact forces are induced from below, while the spring and damping forces act from above. Therefore, the force coefficient is calculated as follows:

$$C = \frac{m_2\ddot{x}_2 - k(x_2 - x_1) - c(\dot{x}_2 - \dot{x}_1)}{(\rho A_{max}U_0^2)/2} \tag{14}$$

This formulation determines the change in the effect of the impact forces on the head.

The evolution of forces predicted by the analytical model, Eq. (9), agrees well with the experimental results. Fig. 7 shows the normalized maximal force coefficient and normalized time at peak impact $t^*_{\max}$ versus normalized natural frequency $\omega_0 h_{cone}/U_0$ for $\beta = 45°$, 60°, and 80° cases. The maximal force coefficient $C_{\max}$ is normalized by C_{rigid}. Contrary to the rigid projectile, the force coefficient is not constant over the impact velocity. This is due to the internal dynamics of the entering body since the spring system response is a function of the excitation frequency, i.e., the impact velocity. This is also different for the head and the projectile's body since they experience different forces and have different masses.

In this study, the eigenfrequency is normalized with h/U_0, which is approximately the impulse frequency. The maximal force coefficient decreases with lower impact velocity or softer springs. Similarly, in Fig. 7b, it can be observed that $t^*_{\max}$ increases with decreasing eigenfrequency or increasing impact velocity. Fig. 7c and d show that $t^*_{\max}$ is similar and experiences only a slight peak force before the rigid case. However, the shape still dominates the maximal force coefficient; see Fig. 7c. Although there is a similar trend, the magnitude of the response differs greatly. The nose force coefficient is lower for low $\omega_0 h/U_0$ compared to the rigid case. It can be observed that the effect of a higher nose angle is greater than that of sharp cones.

4.4. Impulse

The impulse, I, was utilized to estimate impact efficiencies of projectiles with three different half angles, $\beta = [45°, 60°, 80°]$, and three levels of stiffness, rigid, firm, and soft. The impulse, I, is quantified by evaluating the change in momentum throughout the impact, t. The impulse is considered an adequate approximation of the energy losses in the system due to impact (Cooker and Peregrine, 1995). The acceleration measurements were utilized to calculate I using the following integral:

$$I = \int_0^{t_s} F\,dt = \int_0^{t_s} m_1\ddot{x}_1\,dt \tag{15}$$

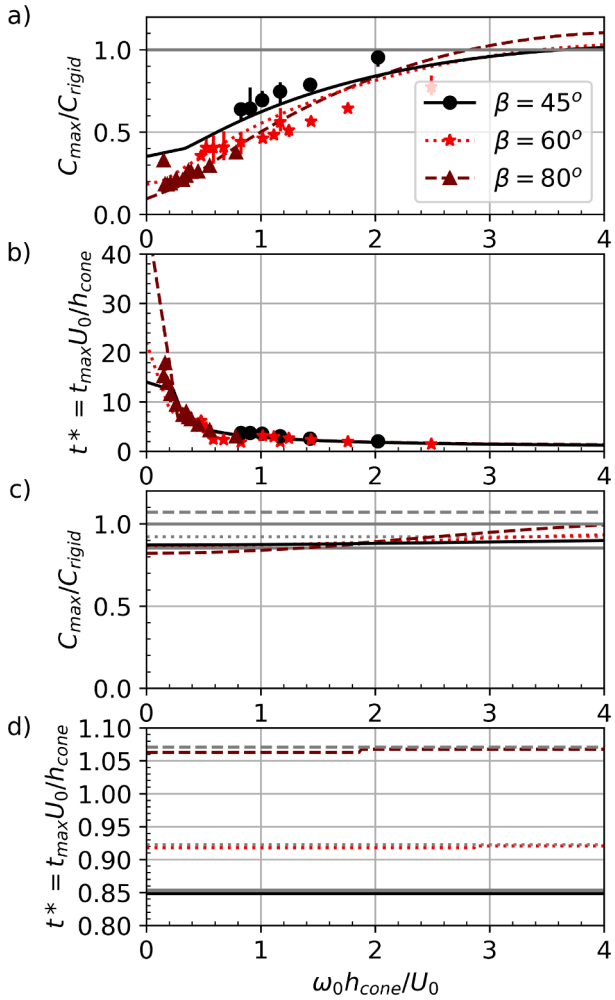

Fig. 7. a,c) Show the maximal force coefficient $C_{\max}$ normalized by the rigid body drag C_{rigid} for the body and the head, respectively. b,d) Show the normalized time to maximal impact over the normalized eigenfrequency. The gray lines are the time to impact for the rigid systems with the relevant angle. The markers with the error bars are the experimental results for the sprung projectiles.

where t_s is set to 100 ms. This specific time duration is selected because the vibrations have attenuated beyond this point and both the rigid and spring cases have reached a steady state. The resulting impulse values are depicted in Fig. 6. It is evident from the experimental (lines) and modeling (markers) results in the figure that the impulses experienced by the sprung projectiles are consistently lower than those for the rigid case. This insignificant finding indicates that integrating spring elements into a projectile does not alter the total impact efficiency. The impulse is weakly quadratic; as expected, the blunt angles experienced higher impulses than the sharp cones.

5. Conclusion

This work illustrates the importance of tuning both geometry and stiffness for water entry. The experimental and modeling results showed that the cone angle was an important tuning parameter for mitigating water-slamming forces, even with the introduction of a spring. As predicted, blunt cones experienced higher slamming forces compared to sharp angles, with the maximal impact force being 20 times higher for a cone angle of 25° than for a cone with an 80° angle. The energy flow analyses showed that blunter cones dissipate energy faster than sharp ones due to their high drag, while sharp cone designs conserved energy, which resulted in prolonged accelerations. However, significant slamming force reductions up to 80 % were achieved when spring compliance was added to a blunt-cone body. Adding a spring in a water-entry system was key for delaying energy dissipation and reducing peak forces simultaneously. The spring provided harmonic energy buffering due to the oscillatory fluctuations between the potential and kinetic energy, which could be controlled by tuning the stiffness. The energy fluctuations were especially pronounced in blunt cones, where the impulse forces were higher than in sharp ones. The intentional integration of compliance into a water-entry body has great promise in providing engineers with a cost-effective tuning parameter besides head geometry, which may be constrained by external factors, to passively control the transmission of the forces and energy in the body during high velocity impact. The findings can be extended to off-shore infrastructures or mechanical systems exposed to violent wave slamming.

CRediT authorship contribution statement

Bart Boom: Writing – original draft, Visualization, Validation, Software, Methodology, Investigation, Formal analysis, Data curation, Conceptualization; **Tadd Truscott:** Writing – review & editing, Visualization, Project administration, Methodology, Investigation, Funding acquisition, Conceptualization; **Frank E. Fish:** Writing – review & editing, Methodology, Investigation, Conceptualization; **Ed Habtour:** Writing – review & editing, Writing – original draft, Supervision, Resources, Project administration, Investigation, Funding acquisition, Formal analysis, Conceptualization.

Declaration of competing interest

The authors declare that they have no known competing financial interests or personal relationships that could have appeared to influence the work reported in this paper.

Acknowledgment

The authors acknowledge funding support by the U.S. National Science Foundation, award no. AWD-022065. The authors also express their sincere gratitude to KAUST and the Splash lab for hosting Bart Boom as a visiting scholar and providing the experimental resources to conduct the research. Additionally, the authors are greatful to Prof. S.T. Thoroddsen and the memebers of the High-Speed Fluids Imaging Laboratory at KAUST for providing access to the water tank, which was essential for the success of this study. Without their support and assistance, this research would not have been possible. Finally, we acknowledge the editorial and technical feedback provided by John Michael Racy, Megan Vandenberg and Thijs Masmeijer.

Appendix A. Model parameters estimation

To estimate C_{ds}, L_p/h, κ, and τ, least squares regression is applied using simulated and experimental data. The continuous relationships for these parameters as a function of the cone angle, β, can be expressed as

$$C_{ds} = a\beta^3 + b\beta^2 + c\beta + d \tag{A.1}$$

$$L_p/h = a\beta^2 + b\beta + c \tag{A.2}$$

$$\kappa = (a\beta^2 + b\beta + c)(\tan\beta)^3 \tag{A.3}$$

$$\tau = a\beta^2 + b\beta + c \tag{A.4}$$

where a, b, c, and d are fitting coefficients given in Table A.2. This results in a continuous model over the full range of cone angles. The steady-state coefficient of drag C_{ds} estimation approach by Baldwin (1971) is utilized for curve fitting using third-order polynomial, as expressed in Eq. (A.1) and Table A.2. The least squares cost function is the difference between the model and simulated data of all trials for a specific cone shape. For example, the residuals between the simulations for all heights are compared with all data trials. The optimal estimates for L_p, κ, and τ

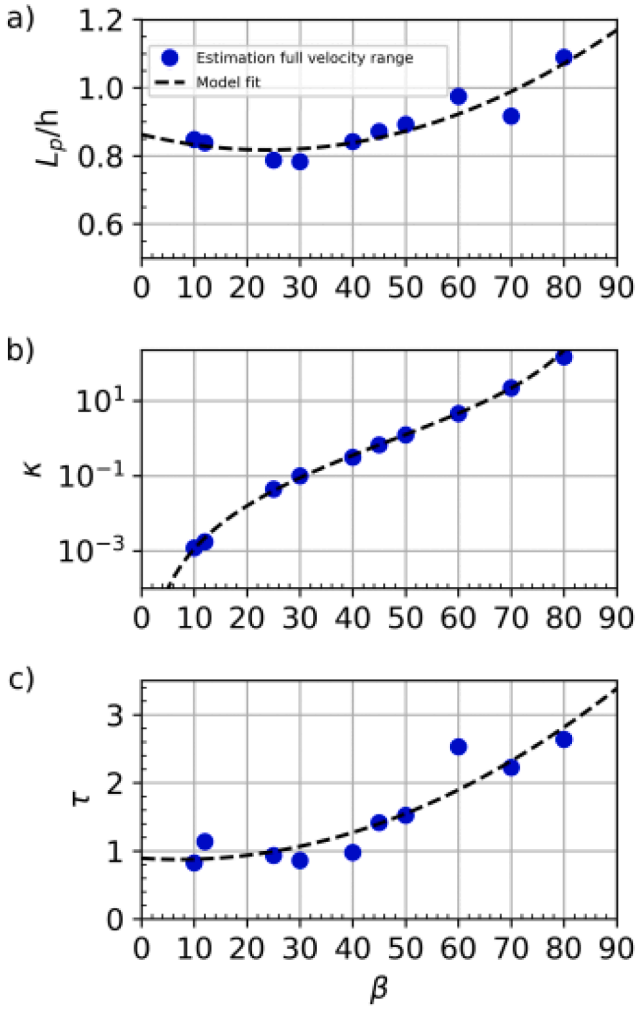

Fig. A.1. Estimating the model parameters by applying least square fitting. The markers and dotted curves are the results from the optimization and the fitted estimations, respectively. a) shows the submerged cone depth at peak acceleration, b) the added mass geometric parameter κ, and c) the decay variable τ.

Table A.1
Comparison data and model for all cone angles for rigid impact an normalized maximal drag coefficient is used and for the sprung case we compare the impact velocity of 4.4 m/s since the maximal drag coefficient changes with impact speed, see Fig. 7.

	Rigid				Firm				Soft			
	C_{max}		t_{max}		C_{max}		t_{max}		C_{max}		t_{max}	
	Data	Model	Data	Model	Data	Model	Data	Model	Data	Model	Data	Model
10	0.20±0.01	0.21	0.898±0.030	0.83	–	0.33	–	1.04	–	0.34	–	1.16
12	0.27±0.11	0.38	0.79±0.00	0.829	–	0.36	–	1.01	–	0.39	–	1.20
25	0.40±0.01	0.58	0.85±0.01	0.82	–	0.73	–	1.18	0.71±0.10	0.58	1.54±0.28	1.71
30	0.53±0.02	0.68	0.85±0.01	0.81	–	0.86	–	1.27	–	0.62	–	2.02
40	0.92±0.02	1.07	0.93±0.02	0.83	–	1.04	–	1.62	–	0.81	–	2.45
45	1.26±0.03	1.36	0.85±0.05	0.85	–	1.16	–	1.79	0.99±0.043	0.68	3.54±0.15	2.99
50	1.59±0.12	1.76	0.89± 0.02	0.87	–	1.32	–	1.99	–	0.85	–	3.48
60	2.93±0.34	3.05	0.89±0.05	0.92	1.70±0.07	1.58	2.54±0.13	2.69	1.34±0.21	1.00	2.46±0.69	4.82
70	4.25±0.52	5.91	0.77±0.11	0.98	–	2.07	–	3.90	–	1.23	–	7.04
80	7.93±0.82	14.92	1.04±0.08	1.07	1.67±0.03	1.54	13.93±0.50	13.22	2.28±0.09	2.79	6.53±0.72	7.36

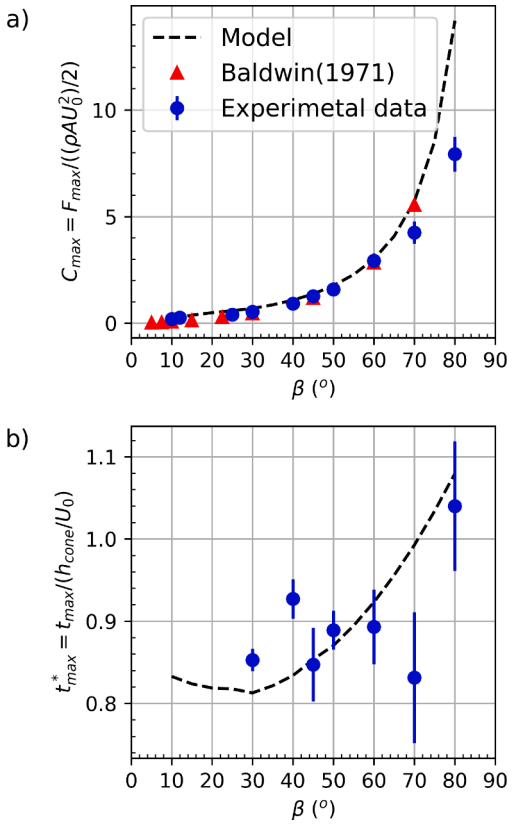

Fig. A.2. Comparison between the model, data from Baldwin (1971) and the experimental data from this study for; a) the maximum drag coefficient $C_{max} = F_{max}/((\rho A U_0^2)/2)$, and the non-dimentionalized time at peak acceleration $t^*_{max} = t_{max}/(h/U_0)$.

are found by minimizing that residual. This leads to a set of parameters for each angle tested, as shown by the markers in Fig. A.1.

The maximal drag coefficient and the time to maximal acceleration correspond well with the collected data see Fig. A.2. Additionally, the maximal drag coefficient is compared to data from Baldwin (1971) and is shown to correspond well with the model. The accuracy of the model is also evaluated in Table A.1

A.1. Eigenfrequency calculation

The eigenfrequency can be utilized to normalize the results in Section 4. Note that this is the damped resonant frequency since the damping and the nonlinear effects are neglected. Calculating the eigenfrequency of the two DoFs undamped homogeneous linear system can be achieved by omitting the nonlinear terms and damping. The procedure

Table A.2
Fitting coefficients found by the least square optimization procedure to estimate the model parameters: C_{ds}, L_p/h, κ, and τ.

	C_{ds}	L_p/h	κ	τ
a	3.4×10^{-2}	7.80×10^{-5}	8.17×10^{-5}	3.67×10^{-4}
b	-2.7×10^{-1}	-3.77×10^{-3}	8.38×10^{-3}	-5.19×10^{-3}
c	8.5×10^{-1}	8.63×10^{-1}	1.21×10^{-1}	8.92×10^{-1}
d	-3.8×10^{-2}	–	–	–

can be found in most vibration textbooks (Meirovitch, 2000).

$$det([K - \omega^2 M]) = 0 \tag{A.5}$$

$$m_1 m_2 \omega^4 - k m_2 \omega^2 - k m_1 \omega^2 = 0 \tag{A.6}$$

The only acceptable solution is given by the following equation

$$\omega_0 = \frac{\sqrt{k m_1 m_2 (m_1 + m_2)}}{m_1 m_2} \tag{A.7}$$

References

Abrate, S., 2011. Hull slamming. Appl. Mech. Rev. 64 (6), 060803.

Antolik, J.T., Belden, J.L., Speirs, N.B., Harris, D.M., 2023. Slamming forces during water entry of a simple harmonic oscillator. J. Fluid Mech. 974, A23.

Aristoff, J.M., Bush, J. W.M., 2009. Water entry of small hydrophobic spheres. J. Fluid Mech. 619, 45-78. https://doi.org/10.1017/S0022112008004382

Baldwin, J.L., 1971. Vertical Water Entry of Cones. Naval Ordinance Lab NOLTR 71-25.

Baldwin, J.L., 1975. Vertical Water Entry of Some Ogives, Cones, and Cusps. National Technical Information Services, US Department of Commerce, ADA009 300.

Belden, J., Speirs, N.B., Hellum, A.M., Jones, M., Paolero, A.J., Truscott, T.T., 2023. Water entry of cups and disks. J. Fluid Mech. 963, A14.

Benschop, H., Breugem, W.-P., 2017. Drag reduction by herringbone riblet texture in direct numerical simulations of turbulent channel flow. volume18 (8), 717–759.

Bhar, K., Chang, B., Virot, E., Straker, L., Kang, H., Paris, R., Clanet, C., Jung, S., 2019. How localized force spreads on elastic contour feathers. J. R. Soc. Interface 16 (160), 20190267.

Boom, B., Truscott, T., Fish, F., Habtour, E., 2025. Dataset: tuning body shape and stiffness to reduce water slamming forces. https://github.com/Illimited-Lab/TwoBodyConeImpactData.

Boom, B., Truscott, T., Fish, F., Summers, A., Habtour, E., 2023. Water entry dynamics of avian inspired divers. In: Smart Materials, Adaptive Structures and Intelligent Systems. Vol. 87523. American Society of Mechanical Engineers, p. V001T06A001.

Carcaterra, A., Ciappi, E., 2000. Prediction of the compressible stage slamming force on rigid and elastic systems impacting on the water surface. Nonlinear Dyn. 21, 193–220.

Chang, B., Croson, M., Straker, L., Gart, S., Dove, C., Gerwin, J., Jung, S., 2016. How seabirds plunge-dive without injuries. Proc. Natl. Acad. Sci. 113 (43), 12006–12011.

Chen, H., Rao, F., Shang, X., Zhang, D., Hagiwara, I., 2013. Biomimetic drag reduction study on herringbone riblets of bird feather. J. Bionic Eng. 10 (3), 341–349.

Chen, H., Rao, F., Shang, X., Zhang, D., Hagiwara, I., 2014. Flow over bio-inspired 3D herringbone wall riblets. Exp. Fluids 55, 1–7.

Chuang, S.-L., Milne, D.T., 1971. Drop Tests of Cones to Investigate the Three-Dimensional Effects of Slamming. DTCI Document No. AD0881183.

Cooker, M.J., Peregrine, D.H., 1995. Pressure-impulse theory for liquid impact problems. J. Fluid Mech. 297, 193–214.

Eager, D., Pendrill, A.-M., Reistad, N., 2016. Beyond velocity and acceleration: jerk, snap and higher derivatives. Eur. J. Phys. 37 (6), 065008.

Elhimer, M., Jacques, N., Alaoui, A. E.M., Gabillet, C., 2017. The influence of aeration and compressibility on slamming loads during cone water entry. J. Fluids Struct. 70, 24–46.

Eliason, C.M., Straker, L., Jung, S., Hackett, S.J., 2020. Morphological innovation and biomechanical diversity in plunge-diving birds. Evolution 74 (7), 1514–1524.
Faltinsen, O., Zhao, R., 1998. Water Entry of Ship Sections and Axisymmetric Bodies. High Speed Body Motion in Water 827.
Gan, W., Zhuang, J., Zhang, Y., Zuo, Z., Xiang, J., 2024. Numerical investigation of the water-entry impact performance of a bionic unmanned aerial-underwater vehicle. Ocean Eng. 303, 117458.
Grady, R.J., 1979. Hydroballistics Design Handbook. Naval Sea Systems Command Hydromechanics Committee, January .
Guo, Z., Chen, T., cheng Mu, Z., Zhang, W., 2020. An investigation into container constraint effects on the cavity characteristics due to high-speed projectile water entry. Ocean Eng. 210, 107449.
Güzel, B., Korkmaz, F.C., 2020. Reducing water entry impact loads on marine structures by surface modification. Brodogradnja 71 (1), 1–18.
Hayati, H., Eager, D., Pendrill, A.-M., Alberg, H., 2020. Jerk within the context of science and engineering-a systematic review. Vibration 3 (4), 371–409.
Koeltzsch, K., Dinkelacker, A., Grundmann, R., 2002. Flow over convergent and divergent wall riblets. Exp. Fluids 33 (2), 346–350.
Korobkin, A.A., Scolan, Y.-M., 2006. Three-dimensional theory of water impact. Part 2. linearized wagner problem. J. Fluid Mech. 549, 343–373.
Li, T., Sigimura, T., 1967. Study of Apollo Water Impact. Volume 1-Hydrodynamic Analysis of Apollo Water Impact Final Report. North American Aviatino Inc. space devision.
Lu, D., Lin, W., Duan, J., Sun, T., 2024. Hydrodynamic performance of a water-air transmedia flying submersible vehicle. Ocean Eng. 307, 118102.
Lyu, X., Yun, H., Wei, Z., 2021. Influence of time interval on the water entry of two spheres in tandem configuration. Exp. Fluids 62, 1–9.
Malleron, N., Scolan, Y.-M., Korobkin, A.A., 2007. Some aspects of a generalized wagner model. In: 22nd International Workshop on Water Waves and Floating Bodies. Vol. 22, p. 4pp.
May, A., 1970. Review of water-entry theory and data. J. Hydronautics 4 (4), 140–142.
McGehee, J.R., Hathaway, M.E., Vaughan, Jr, V.L., 1959. Water-Landing Characteristics of a Reentry Capsule. National Aeronautics and Space Administration.
Mehri, A., Akbarzadeh, P., 2021. Water entry of grooved spheres: effect of the number of grooves and impact velocity. J. Fluids Struct. 100, 103198.
Meirovitch, L., 2000. Fundamentals of Vibrations. McGraw Hill.
Miller, R.W., Merten, K.F., 1952. Hydrodynamic Impact of a System with a Single Elastic Mode II: Comparison of Experimental Force and Response with Theory. National Advisory Comittee for Aeronautics
Paulsen, B.T., de Sonneville, B., van der Meulen, M., Jacobsen, N.G., 2019. Probability of wave slamming and the magnitude of slamming loads on offshore wind turbine foundations. Coastal Eng. 143, 76–95.
Qi, D., Feng, J., Xu, B., Zhang, J., Li, Y., 2016. Investigation of water entry impact forces on airborne-launched AUVs. Eng. Appl. Comput. Fluid Mech. 10 (1), 473–484.
Rabbi, R., Speirs, N.B., Kiyama, A., Belden, J., Truscott, T.T., 2021. Impact force reduction by consecutive water entry of spheres. J. Fluid Mech. 915, A55.
Rockenbauer, F.M., Jeger, S., Beltran, L., Berger, M., Harms, M., Kaufmann, N., Rauch, M., Reinders, M., Lawrance, N. R.J., Stastny, T., et al., 2021. Dipper: a dynamically transitioning aerial-aquatic unmanned vehicle. Robotics: Science and Systems, Vol. 2021, pp. 12–16.
Scolan, Y.-M., Korobkin, A.A., 2001. Three-dimensional theory of water impact. Part 1. Inverse wagner problem. J. Fluid Mech. 440, 293–326.
Sharker, S.I., Holekamp, S., Mansoor, M.M., Fish, F.E., Truscott, T.T., 2019. Water entry impact dynamics of diving birds. Bioinspiration Biomim. 14 (5), 056013.
Shiffman, M., Spencer, D.C., 1951. The force of impact on a cone striking a water surface (vertical entry). Commun. Pure Appl. Math. 4 (4), 379–417.
Shokri, H., Akbarzadeh, P., 2022. Experimental investigation of water entry of dimpled spheres. Ocean Eng. 250, 110992.
Speirs, N.B., Belden, J., Pan, Z., Holekamp, S., Badlissi, G., Jones, M., Truscott, T.T., 2019. The water entry of a sphere in a jet. J. Fluid Mech. 863, 956–968.
Thompson, F.L., 1928. Water-Pressure Distribution on a Seaplane Float. Report-National Advisory Committee for Aeronautics (283-308), 235.
Thompson, W.C., 1965. Dynamic Model Investigation of the Landing Characteristics of a Manned Spacecraft. Vol. 2497. National Aeronautics and Space Administration.
Truscott, T.T., Epps, B.P., Belden, J., 2014. Water entry of projectiles. Annu. Rev. Fluid Mech 46, 355–378.
Truscott, T.T., Techet, A.H., 2009. Water entry of spinning spheres. J. Fluid Mech. 625, 135–165.
Vincent, L., Xiao, T., Yohann, D., Jung, S., Kanso, E., 2018. Dynamics of water entry. J. Fluid Mech. 846, 508–535.
von Karman, T., 1929. The impact on seaplane floats during landing .
Weisler, W., Stewart, W., Anderson, M.B., Peters, K.J., Gopalarathnam, A., Bryant, M., 2017. Testing and characterization of a fixed wing cross-domain unmanned vehicle operating in aerial and underwater environments. IEEE J. Oceanic Eng. 43 (4), 969–982.
Weiss, T., 2014. Gaining intuition for diving birds: wedges and cones as a model for beak-water impact. Virginia Polytechnic Institute Search in.
Wu, Z., Zhang, C., Wang, J., Shen, C., Yang, L., Ren, L., 2020. Water entry of slender segmented projectile connected by spring. Ocean Eng. 217, 108016.
Xu, G.D., Duan, W.Y., Wu, G.X., 2011. Numerical simulation of water entry of a cone in free-fall motion. Q. J. Mech. Appl. Math. 64 (3), 265–285.
Zimmerman, S., Abdelkefi, A., 2020. Enhanced design considerations on the buckling and dynamics of gannet-inspired systems during water entry. Bioinspiration Biomim. 16 (2), 026011.
Zimmerman, S., Ceballes, S., Taylor, G., Chang, B., Jung, S., Abdelkefi, A., 2019. Nonlinear modeling and experimental verification of gannet-inspired beam systems during diving. Bioinspiration Biomim. 14 (2), 026002.